Chapter-3

3 Biogenic Synthesis of Dual-emission Chlorophyll-rich Carbon Quantum Dots for Detection of Heavy Toxic Metal Ions – Hg (II) and As (III) in Water and Mouse Fibroblast Cell Line NIH-3T3.

3.1 Introduction

3.1.1 Source of Water Pollutant

Water is the most critical resource for sustaining life and supporting the life systems of organisms. It is essential for human consumption to be secure, convenient, sufficient, and free from contamination. However, water bodies worldwide are facing various forms of pollution, posing serious threats to human health and the aquatic ecosystem. Water pollution can occur in different ways, including the presence of pathogens, thermal pollution, radioactive pollution, inorganic pollutants, organic pollutants, microbiological pollutants, microplastic pollutants, suspended solids, and sediments[151]. One of them, heavy metals (HMs), naturally occurring in different oxidation states, molecular structure, and complex forms, are present in the Earth's crust with different molar concentration. Some HMs, such as Cd, Pb, Mo, Co, Hg, and As, are classified as non-essential due to their high toxicity, carcinogenicity, and mutagenicity to plants and animals. These HMs cannot be degraded or metabolized by natural processes[152]. While essential elements like Cu, Zn, and Cr are necessary in trace amounts, higher concentrations of these elements are poisonous[153]. Heavy metal pollution originates from geological, industrial, medicinal, and agricultural activities, including mining, factories, batteries, and metal plating.

Two of the most prevalent metalloids on Earth, arsenic and mercury, pose global public health problems and are harmful to plant and animal life. Arsenic exists in various chemical forms and oxidation states, with arsenites (AsO_3^{3-}), arsenates (AsO_4^{3-}), monomethyl (MMA), and dimethyl (DMA) metabolites being common forms causing human health issues[154], [155].

Arsenic is naturally present in more than 200 minerals, some of which are volatile and highly soluble in water, leading to its continuous release into groundwater. Many countries, including Bangladesh, India, China, the United States, and others, have high levels of naturally occurring inorganic arsenic in their groundwater[156], [157]. Exposure to arsenic occurs through drinking water, irrigation of crops with contaminated water, and cooking food with contaminated water. In addition to contaminated groundwater, arsenic can also be found in fish, seafood, pig, chicken, milk products, and wheat[158]. Even at relatively low concentrations, arsenic exposure can lead to various illnesses such as hepatocellular carcinoma, melanosis, hyperkeratosis, diabetes mellitus, hypertension, malignancies, cirrhosis, liver fibrosis, and parenchymal cell damage[159].

Mercury, a naturally occurring metal, can constitute up to 86% of the mineral cinnabar's composition. Humans have been extracting mercury from cinnabar since ancient times. While natural processes such as rock weathering and volcanic activity release mercury into the environment, human activities such as coal-fired power plants and industrial waste disposal are the primary sources of mercury pollution[160]. Once released, mercury can be transformed by microorganisms in soil and aquatic environments into methylmercury (MeHg), a highly toxic form[161]. Due to its dangerous nature, mercury should not be touched, inhaled, or consumed, as each exposure allows it to accumulate in the body, making it difficult to eliminate. Mercury easily enters the food chain, with methylmercury accumulating in organisms and becoming more concentrated as it moves up the food chain. Predatory fish, which are consumed by humans, often have significantly higher levels of methylmercury compared to the surrounding water. This bioaccumulation of mercury can lead to harmful effects on both human health and fish-eating species[162]. Excess mercury exposure can result in kidney failure, brain damage, and various illnesses. The toxicity of mercury is influenced by factors such as the level of exposure, the specific chemical form, the individual's age, gender, genetics, and diet[163].

3.1.2 Techniques for detection of heavy metals in water

Detecting and identifying these harmful heavy metals at extremely low concentrations in water is a significant challenge. Various atomic spectroscopic methods, including absorption, emission, and mass spectroscopy, have been employed to address this issue[164]. These methods offer detection limits below the standards set by organizations like WHO (World Health Organization) and EPA (Environmental Protection Agency). However, they are not suitable for on-site diagnostics due to their long run times, high costs, and cumbersome equipment requirements[165]. As alternatives, electrochemical methods, surface-enhanced Raman spectroscopy, fluorescence spectroscopy, and chemiluminescence have been explored as low-cost options. Fluorescence technologies are particularly favoured due to their rapid response time, high sensitivity, specificity, accuracy, and real-time analysis capabilities[166]. Recent research has focused on utilizing carbon quantum dots (CQDs), graphene oxide (GO), semiconducting carbon dots, and other nanomaterials as fluorescence markers in detection systems[167]. CQDs, zero-dimensional carbon materials with sizes less than 10 nm, have gained attention due to their desirable properties such as photoluminescence, chemical stability, biocompatibility, easy functionalization, cost-effectiveness, and low toxicity[168]–[170]. However, semiconducting carbon dots, like CdSe, CdSe/ZnS, and InP/ZnS, have drawbacks including high toxicity, heavy metal usage in their production, restricted use in clinical studies, and relatively high synthesis costs[171], [172]. In this study, we focus on a novel class of materials known as heavy metal-free CQDs, which offer absorbing characteristics, low toxicity, good solubility, and stable photoluminescence[171], [173].

3.1.3 Properties of CQDs

Researchers have recently explored the synthesis of carbon dots from natural resources such as orange peel[174], soy milk[175], watermelon peel[176], garlic[177], and other plant parts.

These carbon dot materials primarily consist of carbon, hydrogen, and oxygen, with additional nitrogen, sulphur, and other heteroatoms introduced through surface modification to enhance their properties[178]. The carbon dots can exist in crystalline and amorphous forms and exhibit sp^2 and sp^3 hybridized carbon centers, allowing for both σ and π bonding. Two main synthesis approaches, the "top-down technique" (e.g., laser ablation, arc-discharge method, electrochemical exfoliation, oxidative acid treatment) and the "bottom-up approach" (e.g., hydrothermal, microwave, thermal combustion, ultrasonic), are used to produce carbon dots[179]–[181]. Hydrothermal synthesis, known for its affordability, simplicity, and environmental benefits, has been widely employed in various applications such as bioimaging[178], drug delivery[170], sensing[173] (including heavy metals, medicines, small and macromolecules, cations, anions, cells, and bacteria), antibacterial agents[182], fingerprint detection[183], light-emitting diodes[184], and more.

In this study, we synthesized CQDs with dual emission using one step solvothermal method and utilized them to detect Hg^{2+} and As^{3+} ions in water and living cells. We used the leaves of the apocynaceae family plant known as the frangipani or plumeria rubra, as a precursor for the synthesis of the CQDs. These plants are native to North America, Mexico, and the Caribbean, these species can also be found growing in warm climates[185]. The extract of the leaves of plumeria rubra were prepared in proponol-1 solution and used for solvothermal synthesis at 160°C and 220°C. The resultant CQDs formed stable dispersions in water. We observed a strong dependence of the optical properties of the CQD on the synthesis temperature. We found that the CQDs synthesized at 160°C showed dual emission, around blue green-green region (485 nm) and red region (676 nm), while the CQDs synthesized at 220°C showed emission only in the blue-green region. We observed that peak at 485 nm showed strong dependence on the excitation energy while there was no effect on the peak at 676 nm. Addition of As^{3+} ions enhanced the peak at 485 nm for CQDs synthesized at 160°C and 220°C. Addition of Hg^{2+} ions

quenched the red emission peak at 676 nm for CQDs synthesized at 160°C only. Fluorescence lifetime measurements showed that the quenching of fluorescence on addition of Hg^{2+} ions were due to combined effect of static and dynamic quenching mechanism. To understand the effect of metal ions on the fluorescence of the CQDs, we investigated the interaction of the metal ions with the CQDs using X-ray photoelectron spectroscopy. We observe that the Hg^{2+} and As^{3+} ions are binding to oxygen functional groups present on the CQDs which alters the fluorescence of the CQDs. Dual emission CQDs synthesized using various green precursors are mostly used as ratio-metric sensor for detecting only one type of metal ion. In our case the dual emission CQDs synthesized at 160°C, can be used for sensitive and simultaneous and detection of Hg^{2+} and As^{3+} ions in water. We have also utilized these CQDs to detect the As^{3+} and Hg^{2+} ions in human cells.

3.2 Results and Discussion

3.2.1 Optical Characterization of CQDs

CQDs synthesized at 160˚C and 220˚C were characterized using different techniques. Figure 3.1(a) shows the UV-vis spectra of the plumeria leaf extract and the CQDs. The absorption spectra of the extract and the CQD160 are quite similar, with broad peak around 265-330 nm and weak peaks at 418 nm and 676 nm. The broad peak may be convolution of absorption peaks due to π- π* transitions of C=C bond usually observed around 250-270 nm, and the absorption peak for n-π* transition of C-O bonds observed at 280 nm. The weak peaks at 418 nm and 670 nm correspond to the chlorophyll moiety[186]. The CQDs synthesized at 220°C show only one peak at 280 nm. The absorption peak at 418 nm and 676 nm is due to the B and Q band. The photoluminescence emission spectra of CQD160 and CQD220 are shown in Figure 3.1(b). The PL spectra was acquired with excitation wavelength of 410 nm. We observe two distinct emission peaks at 485 nm and 676nm. The broad emission peak around 485 nm is

characteristic of CQDs, while the sharp peaks at 676 nm and 730 nm indicate the presence of chlorophyll moiety (molecular states)[187]. The emission intensity in the blue-green region increased as the synthesis temperature, while intensity in the red region decreased and eventually disappeared at 220°C. This can be attributed to the denaturation of the chlorophyll structure at high temperatures. Similar temperature dependence was observed for CQDs synthesized from banana leaf and holly leaf precursor[85], [188].

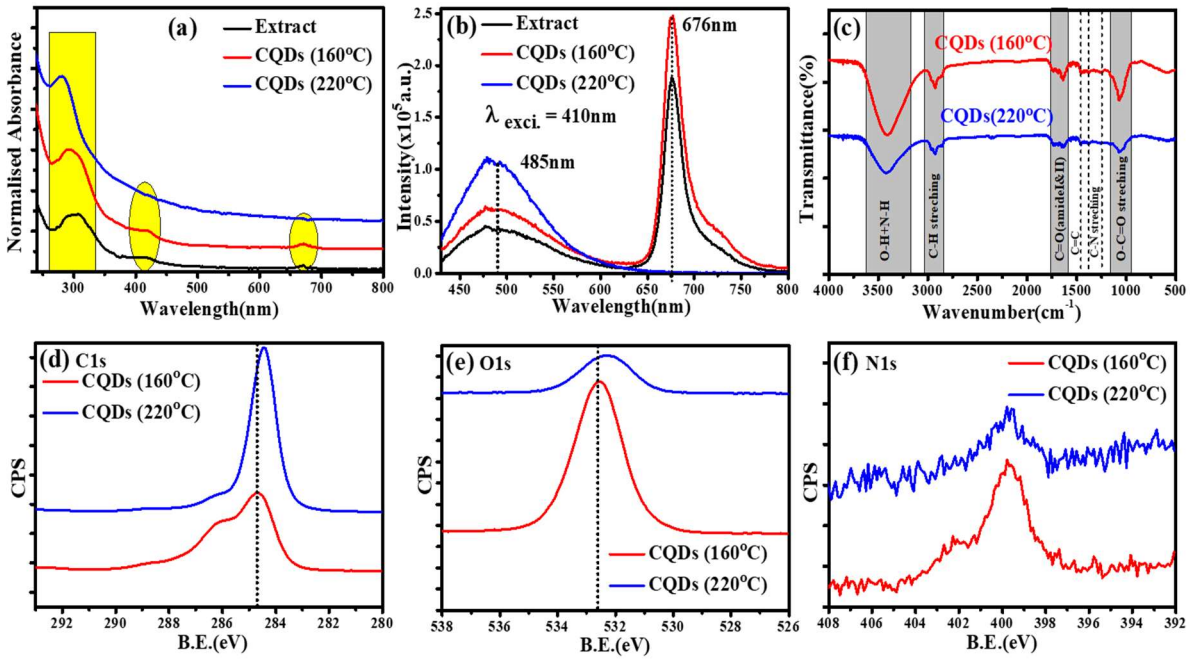

Figure 3. 1 (a) UV-Vis Absorption spectra, (b) Emission spectra, (c) FTIR spectra of CQDs prepared at temperature 160ºC, and 220ºC. (d) C1s, (e) O1s (f) N1s High-resolution XPS photoelectron peaks of CQDs as synthesized at temperature 160ºC, and 220ºC.

Figure 3.1(c) shows the Fourier-transform infrared (FTIR) spectra of the CQDs. The O-H and N-H stretching vibrations resulted in a broad peak at 3422cm^{-1}, while the C-H stretching vibrations produced a sharp absorption peak at 2922cm^{-1}. The C=O stretching modes of vibration (carbonyl groups) correspond to the C=C or aromatic ring stretching modes at 1736 cm^{-1} and 1641 cm^{-1}, respectively [189]. Additionally, the C-C-O stretching vibration produced a peak at 1258 cm^{-1}, while the C-N stretching vibration resulted in a peak at 1072 cm^{-1}. These

results demonstrate that CQDs are decorated with various functional groups, including nitrogen, oxygen, and carbon atoms. Many oxygen-containing and some nitrogen-containing functional groups can be observed on the surface of CQDs. Due to the high concentration of oxygen-containing functional groups, CQDs exhibit excellent solubility in water. The chemical composition of CQDs synthesized at different temperatures was investigated through X-ray photoelectron spectroscopy (XPS) analysis.

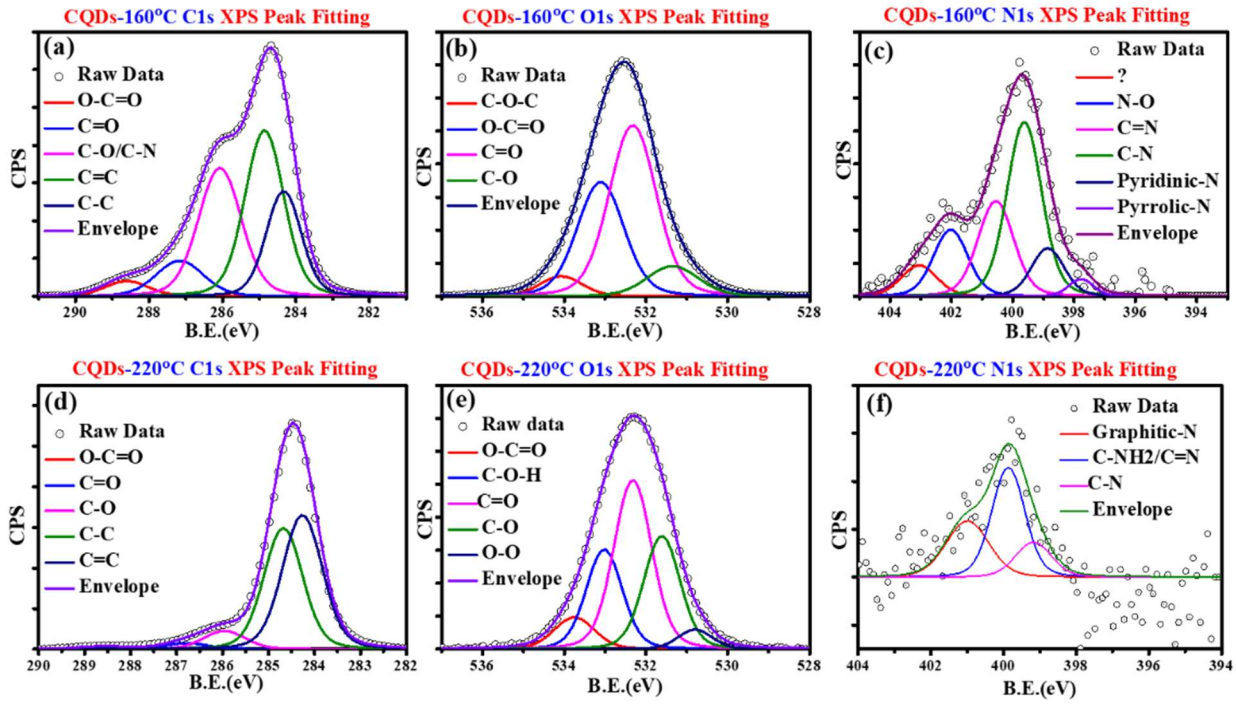

Figure 3. 2 Deconvolution of photoelectron XPS peaks with different synthesized temperature. (a), (b), and (c) shows the deconvolution of C1s, O1s, and N1s photoelectron spectra of as synthesized CQDs at 160°C. (d), (e), and (f) shows the deconvolution of C1s, O1s, and N1s photoelectron spectra of as synthesized CQDs at 220°C.

The survey spectra in Figure 3.4(a) show the XPS signals obtained over a range of photon energies from 0 to 1350 eV. The high-resolution photoelectron peaks of C1s, O1s, and N1s of CQDs at different synthesis temperatures are displayed in Figure 3.1(d-f) respectively. On inspection, we observe a change in the peak shape and a small peak shift for C1s peak. The

intensity of O1s peak decreased sharply when synthesis temperature was increased to 220°C. We observe a very weak N1s peak whose intensity decreases further with increase in synthesis temperatures. To get information about different species contributing to the C1s, O1s and N1s photoelectron peaks, we deconvoluted the peaks using peak fitting software Casa XPS. The deconvoluted peaks for C1s, O1s and N1s is shown in Figure 3.2. For the C1s, we observe the following components O-C=O, C=O, C-O-C, C-O/C-N, C=C/C-C bonding. For CQD160, the relative concentration of C=C/C-C bonds is the highest (50%) followed by C-OH at 30% (see Table 3.1). For the CQD220 we observe the relative concentration of C=C/C-C increases to ~90% while that of C-OH bond reduced to ~7%. For the O1s, we observe the following components C-O-C, O-C=O, C-OH, C=O, C-O bonding. For CQD160, the relative concentration of C=O is highest at 44% followed by C-OH at 33%. For CQD220, the overall oxygen decreases and the relative concentration of C-OH also decreases.

(a) C1s	**CQDs-160°C**		**CQDs-220°C**	
	Position (eV)	**% Area**	**Position (eV)**	**% Area**
O-C=O	288.6	3.7	288.6	1.0
C=O	287.1	9.3	286.8	2.3
C-O/C-N	286.0	30.7	286.0	6.9
C=C	284.6	30.8	284.7	42.9
C-C	284.3	20.4	284.3	47.9

(b) O1s	**CQDs-160°C**		**CQDs-220°C**	
	Position	**% Area**	**Position**	**% Area**

	(eV)		(eV)	
C-O-C	534.15	5.8	-	-
O-C=O	533.55	9.9	533.78	7.9
C-O-H	532.9	32.8	532.98	22.3
C=O	532.2	44.5	532.2	39.9
C-O	531.2	7.5	531.58	25.6
O-O	-	-	530.78	4.1

Table 3. 1 (a), and (b) The C1s, O1s peak positions obtained after peak fitting. The error ± 0.2 eV for peak C1s and O1s peak of CQDs at different synthesis temperature.

Thus, as the synthesis temperature is being increased to 220°C the fraction of carbon atoms bonded to hydroxyl group decreases. For the N1s, we observe the following components C=N, C-N, pyridinic, pyrollic bonding configurations. The N1s for the CQD220 is so weak that the peak fit is not very reliable. Thus, from XPS we can conclude that in the CQDs, the carbon is bonded with mostly oxygen containing functional groups with a very small fraction of them bonded to nitrogen groups. As the synthesis temperature is increases to 220°C, the number of oxygen and nitrogen functional groups reduce dramatically. The CQDs are becoming more hydrophobic with increase synthesis temperature.

The structural morphology of the CQD160ºC was examined using transmission electron microscopy (TEM). The TEM image shown in Figure 3.3(a), reveals that most of the CQDs have a quasi-spherical shape with a uniform size distribution. The presence of diffuse rings in the selected area electron diffraction (SAED) pattern, inset of Figure 3.3(a), indicated the amorphous character of the CQD160. The size distribution of the CQD160 was determined and is presented in Figure 3.3(b), with an average size of 3.37± 0.04nm.

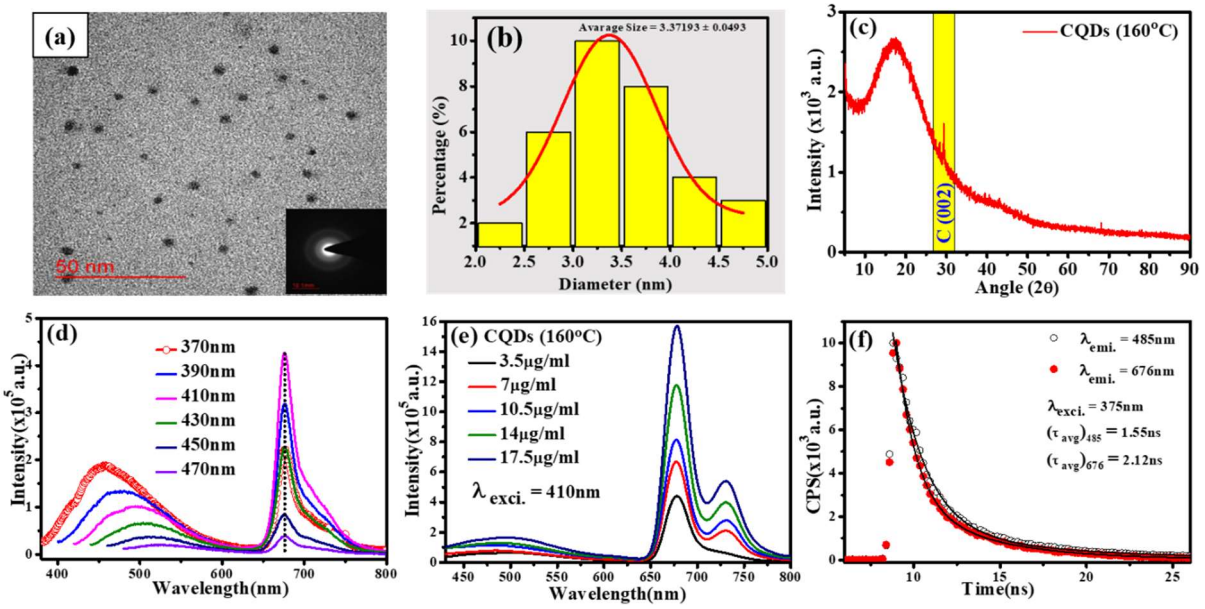

Figure. 3. 3 (a) TEM image of CQD160, inset: SAED pattern of CQD160. (b) bar diagram of CQD160 as size distribution. (c) XRD pattern of as synthesized CQD160. (d) Excitation concentration-dependent PL spectra of CQD160 (e) Concentration-dependent PL spectra of CQD160 by using excitation 410nm. (f) TRPL spectra of CQD160.

The X-ray diffraction (XRD) pattern of the CQD160, shown in Figure 3.3(c), exhibited a broad peak with a less pronounced peak at 18° and 29°. The reflection planes (002) present in the pattern at 29° suggested the presence of CQDs with a sp^2 graphitic-like structure[190]. Figure 3.3(d) shows the photoluminescence (PL) spectrum of CQD160 as a function of excitation wavelength. For this measurement the concentration of 3.5µg/ml and the excitation wavelength were varied from 370 nm to 470 nm. We observe that the emission peak at 485 nm experiences a red shift as the excitation wavelength increases, while the peak at 676 nm has no dependence on excitation wavelength. In addition, to the red shift of the 485 nm peak, which is characteristic of CQDs, we also observe a steady decrease in the intensity of the 485 nm peak. On the other hand, the intensity of the 476 peak initially increases for excitation wavelengths 370-410 nm but starts decreasing when the excitation wavelength is further increased. For excitation wavelength 430 nm and above the intensity of both peaks start decreasing. The

maxima for 485 nm and 676 peak is observed at excitation wavelength 370 nm and 410 nm respectively. In the subsequent measurements we have either used 350 nm or 410 nm as the excitation wavelength for PL measurements. Figure 3.3(e) shows the PL spectra of CQD160 as function of concentration for 410 nm excitation wavelength. The concentration of the CQDs was varied from 3.5 µg/ml to 17.5 µg/ml. With increasing concentration, a weak peak at 730 becomes sharper.

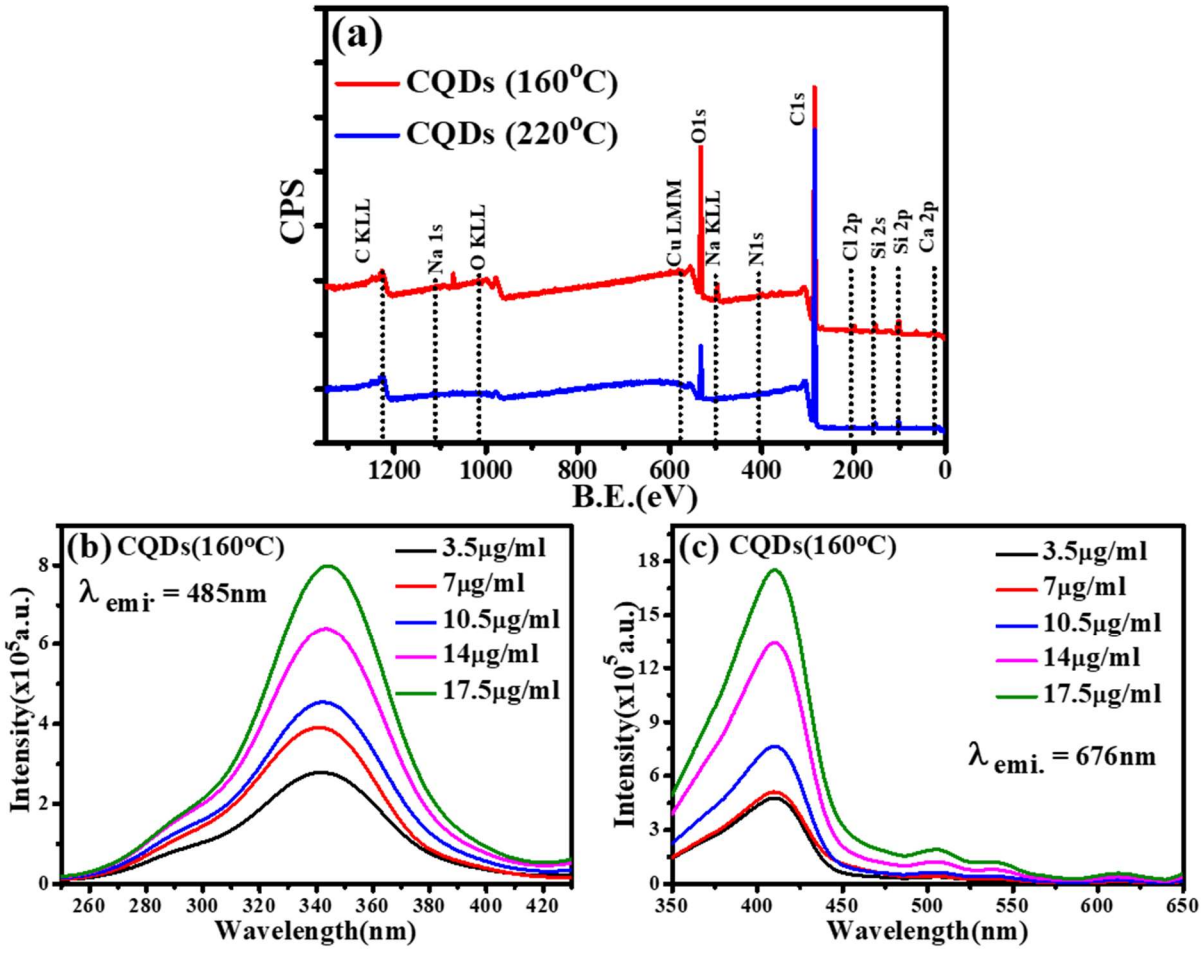

Figure 3. 4 (a) XPS survey spectra of CQDs as synthesized temperature at 160°C and 220°C. (b), and (c) Shows the concentration dependent excitation spectra of CQDs160 corresponding emission wavelength as 485nm and 676nm.

The excitation spectra of CQDs as function of concentration is shown in Figure 3.4(b) and (c). The excitation spectra were recorded for emission at 485 nm and 678 nm separately. We

observe the intensity of the excitation spectrum increased with increasing concentration. The TRPL data for the CQD160 was obtained for excitation wavelength 385 nm. The decay characteristics was measured for 485 nm and 676 nm emission peaks. The PL decay curves were fitted with bi-exponential curves. The PL decay curves were fitted with bi-exponential function which yielded two lifetimes.

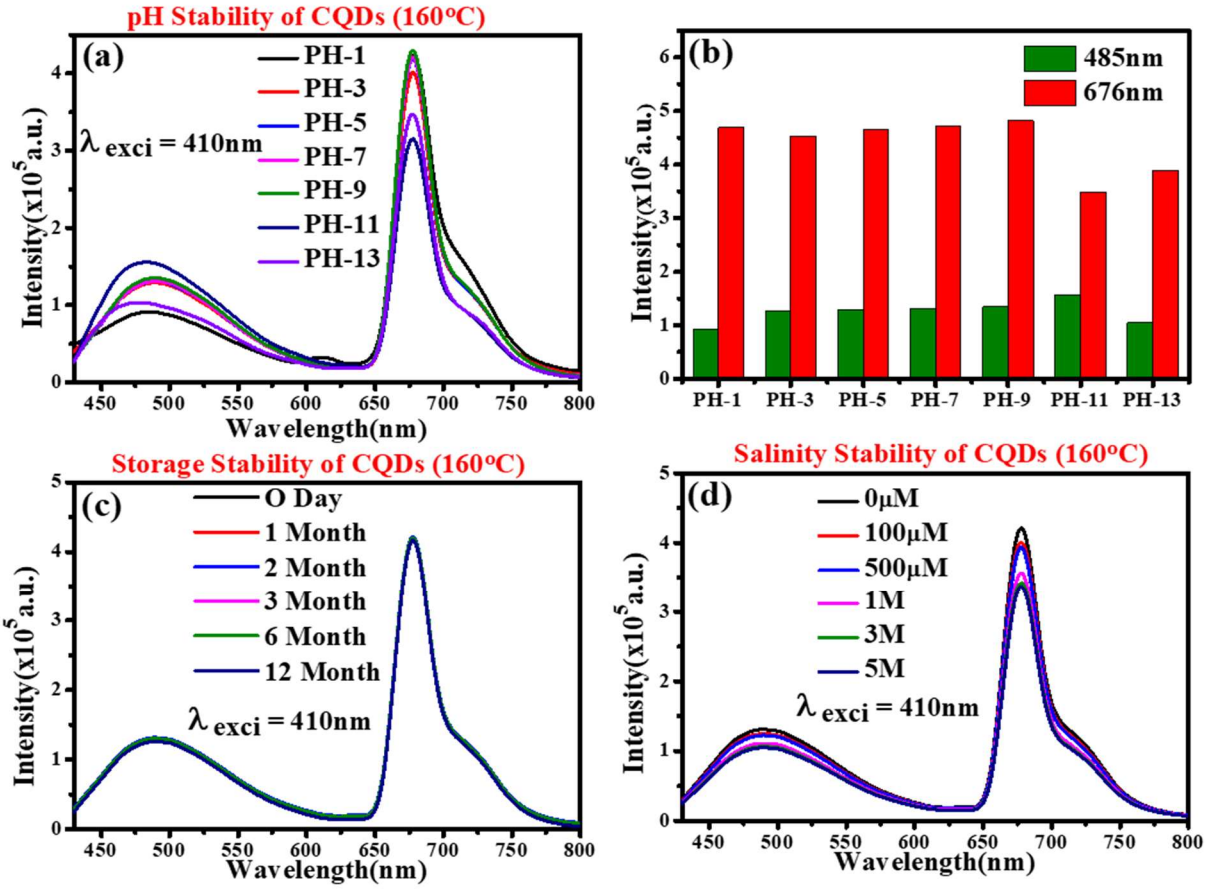

Figure 3. 5 Stability measurement of CQDs160. (a) measurement of PL emission at different pH value, (b) Bar diagram of pH stability of CQDs160 corresponding 485nm and 676nm. (c) PL emission stability of CQDs160 with respect to storage time. (d) Salinity stability of CQDs160 at different molarity value.

The average lifetime for 485 nm and 676 nm emission peak is 1.55 ns and 2.12 ns respectively. Stability of the CQD160 with respect to pH, storage time and salinity was also studied (Figure 3.5). When pH is increased from 1 to 13, the intensity of 485 slowly increases. On the other

hand, for peak 676 nm stays nearly constant over in the range pH 1-9 and then decreases sharply (see Figure 3.5(a) and (b)). The pH sensitivity of the florescence may be due to reversible protonation and deprotonation of the functional groups on the CQDs. The aging effect on the stability of the CQD160 was also studied. Figure 3.5(c) shows the PL emission of CQD160 over a period of one year.

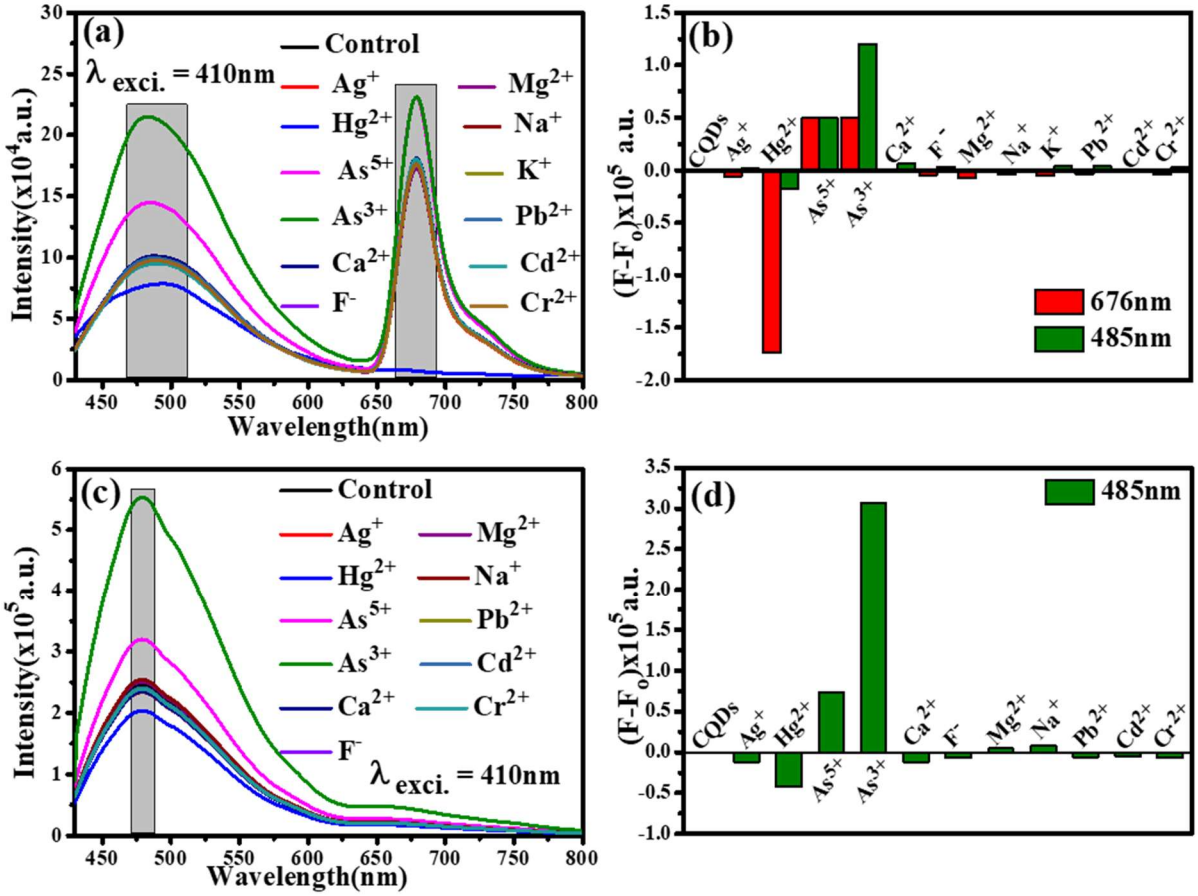

Figure 3. 6 (a) showing the selectivity of metal ions (Hg^{2+} and As^{3+}) using as synthesized CQD160. (b) Bar diagram of metal selectivity by using as synthesized CQD160. (c) showing the selectivity of As^{3+} metal ions using as synthesized CQD220. (d) Bar diagram of metal selectivity by using as synthesized CQD220.

We do not observe any noticeable change in the PL spectra of these CQDs. Moreover, CQD160 exhibited good salinity stability, with only minor changes observed at concentrations above 3 molar (see Figure 3.5(d)). These findings suggest that CQDs synthesized at 160°C exhibit

excellent stability under various environmental conditions, making them a promising candidate for various applications.

3.2.2 Sensing of $As^{3+}$and Hg^{2+}

We utilised the CQD160 and CQD220 to detect various toxic metal ions in water. Figure 3.6(a) and (c) shows the PL spectra of the CQDs synthesized at 160°C and 220°C after addition of different metal ions at concentration of 100µM

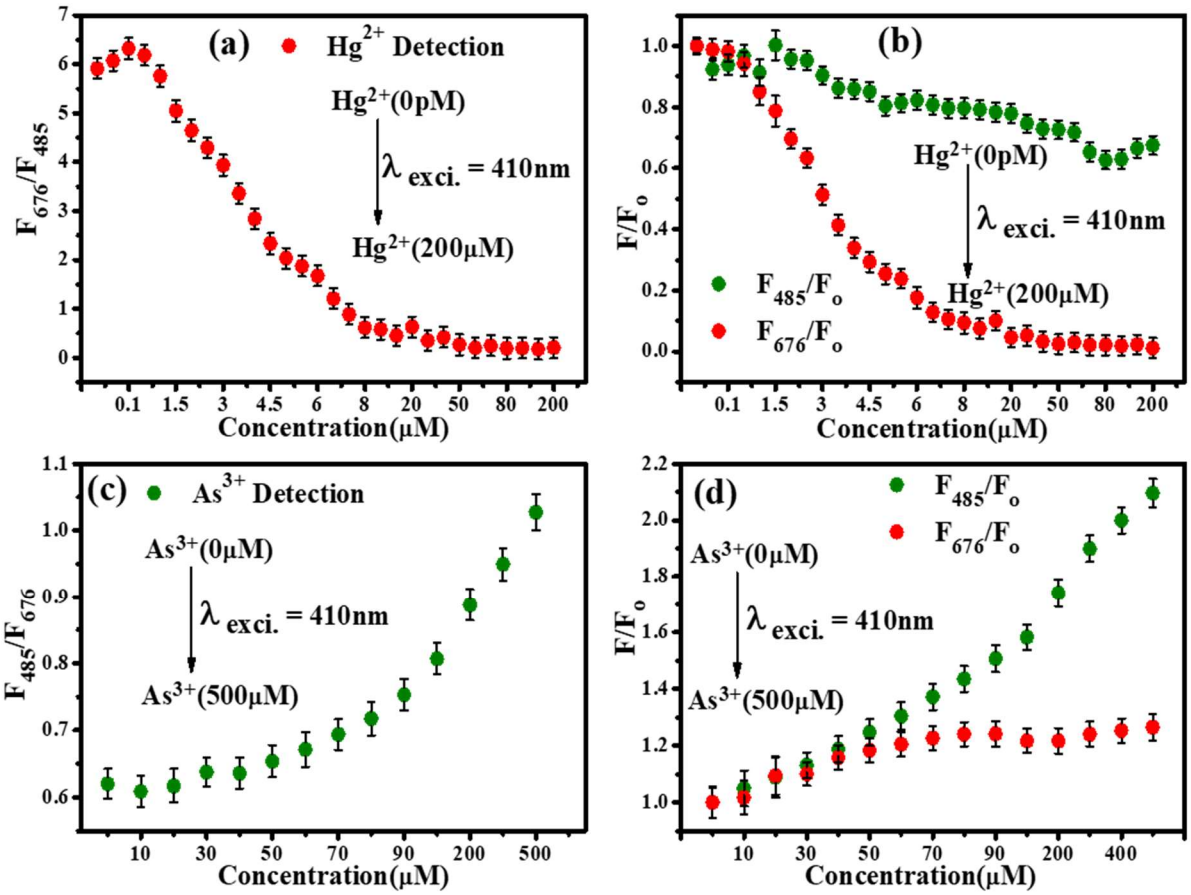

Figure 3. 7 Intensity ratio plot of CQD160. (a) F_{676}/F_{485} vs Concentration plot of Hg^{2+} detection. (b) shows the F/F_0 vs concentration graph corresponding 485 nm and 676 nm peaks with addition of Hg^{2+} ions. (c) F_{485}/F_{676} vs Concentration plot of As^{3+}detection. (d) shows the F/F_0 vs concentration graph corresponding 485 nm and 676 nm peaks with addition of As^{3+} ions. After adding the metal ions, we monitored the change in intensities of PL peaks at 485

nm and 676 nm. Figure 3.6(b) and 3(d) shows the bar chart depicting the variation of peak intensities at 485 nm and 676 nm for CQD160 and CQD220 respectively. For CQD160 we observed little or no change in the PL peaks for most of the metal ions except Hg^{2+} and As^{3+} ions. A profound but opposite behaviour is observed in PL intensities for Hg^{2+} and As^{3+} ions. When Hg^{2+} ions are added, the peak at 676 nm gets quenched rapidly while in the case of As^{3+} ions the peak at 485 nm is enhanced. The ratio of peak intensities (F_{676}, F_{485}) and normalized peak intensity (485, and 676 nm) after addition of metal ions is shown in Figure 3.7. Interestingly, our result is very different from that observed for banana leaves derived CQDs. Bayazeed et. al. had observed quenching and enhancement effect in the same peak at 676 nm upon addition of Hg^{+} and As^{3+} ions to CQD160 derived from banana leaves[85].

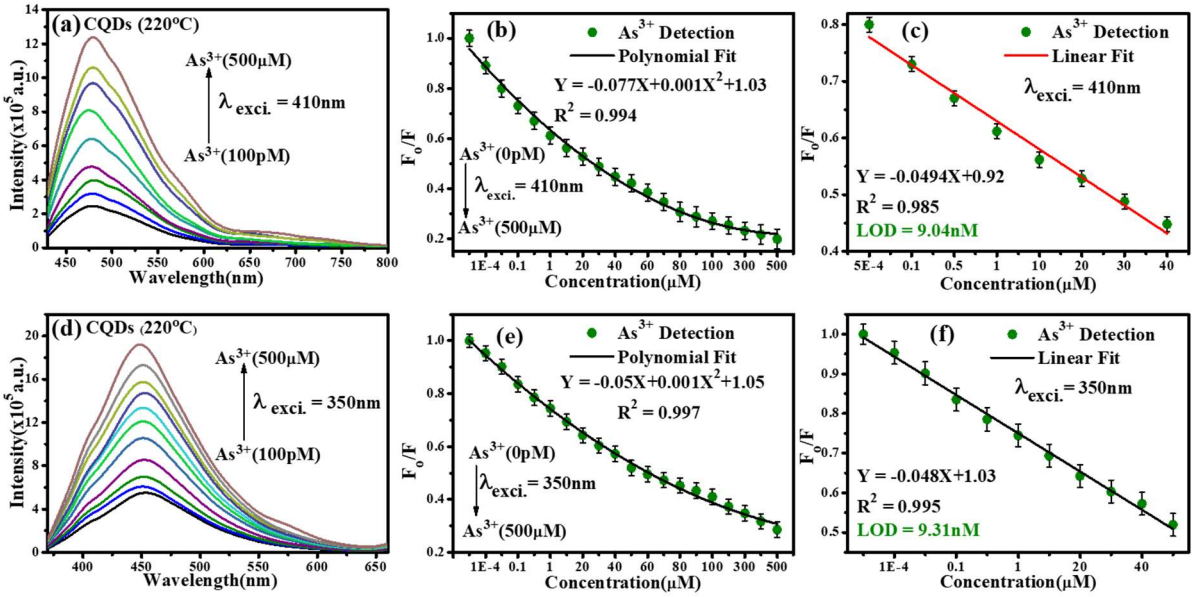

Figure 3. 8 (a) PL emission spectra of CQD220 derived by As^{3+} by using excitation wavelength as 410nm, (b) showing the polynomial fitting between F_o/F vs concentration, (c) plotting the linear range of As^{3+} detection and find the LOD value as 9.04nM, (d) PL emission spectra of CQD220 derived by As^{3+} by using excitation wavelength as 350nm, (e) showing the polynomial fitting graph between F_o/F vs concentration, (f) plotting the linear range of As^{3+} detection and find the LOD value as 9.31nM.

The starting precursor thus plays an important role in determining the optical response of the CQD160 to the toxic metal ions. Our CQD160 derived from plumeria leaves can thus be used as a true ON-OFF sensor for selectively detecting Hg^{2+} and As^{3+} ions in water. When the same tests were repeated for CQD220, we observe quenching of 485 peak only on addition of As^{3+} ions and no appreciable change when other metal ions are added. Thus, we can use either CQD160 and CQD220 for detection of As^{3+} ions while the Hg^{2+} ions can be detected with CQD160 only. We conducted detailed PL measurements for both CQD160 and CQD220 as function of Hg^{2+} and As^{3+} ions concentration. The results for CQD160 are discussed in the following paragraphs but the result for CQD220 is shown in the Figure 3.8.

To determine the limit of selection (LOD), the PL emission spectra of CQD160 was recorded for different concentration of $Hg^{2+}$and As^{3+} using as excitation wavelength 410 nm. Figure 3.9(a) and (c) shows the PL emission of CQD160 as a function of Hg^{2+} and As^{3+} concentration respectively. When the Hg^{2+} ion concentration is increased, the peak intensity at 676 nm decreases while the peak at 485 nm shows little change. When the concentration of Hg^{2+} ions become greater or equal to 200 μM, the peak at 676 nm is completely quenched. Figure 3.9(b) shows the Stern Volmer (SV) plot for sensing of Hg^{2+} ions. It shows the relationship between F_o/F with Hg^{2+} concentration, where F_0 and F are the PL intensity of 676 nm peak for CQD160, without and with Hg^{2+} ions. The F_0/F plot varies linearly for small values of concentration and starts to bend upwards for higher concentrations of Hg^{2+} ions. From the linear region between 2.5μM to 6μM, we estimated the LOD value as 0.99 nM (Figure 3.9(c)). In contrast to Hg^{2+} ions, when As^{3+} ions are added to the CQD160 solution, the intensity of peak at 676 nm remains nearly unchanged but the intensity of peak at 485 nm gets enhanced. The variation of F_o/F as function of As^{3+}concentration is shown in Figure 3.9(e), where F_o and F are the PL intensities of peak 485 nm for CQD160 without and with As^{3+}ions, respectively. From the SV plot we can

see that for As^{3+} ions the enhancement varies linearly for a large range of concentration from 5 µM to 300 µM.

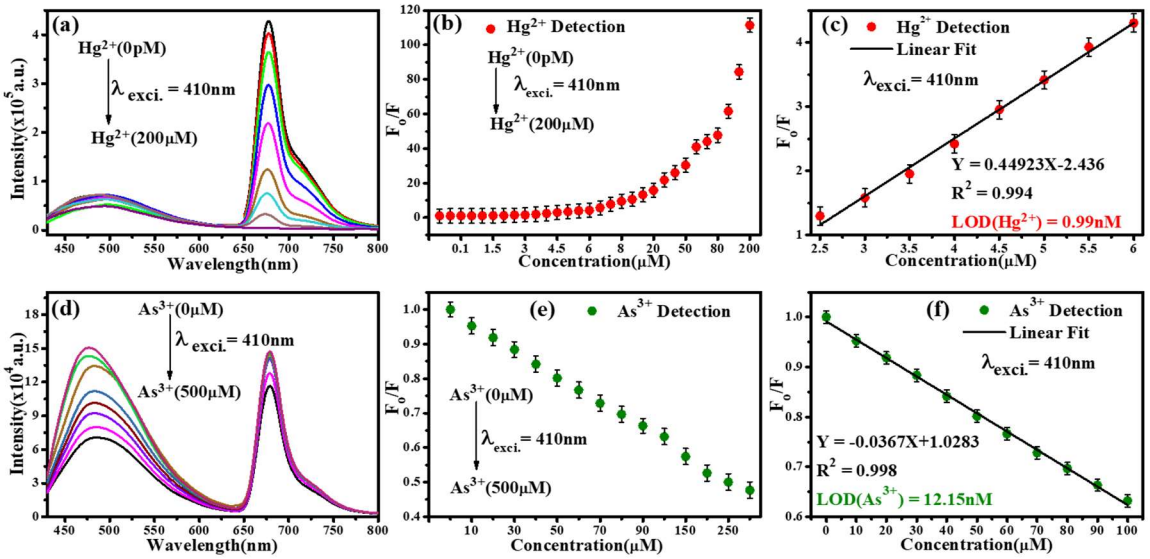

Figure 3. 9 (a) PL emission-based sensing of Hg^{2+} derived by CQD160 using excitation as 410 nm. (b) F_0/F vs concentration plot of Hg^{2+} from 0 pM to 200 mM. (c) Drawn the linear correlation range of Hg^{2+}ions detection. (d) PL emission spectra of CQD160 derived by As^{3+} by using excitation wavelength as 410nm. (e) The graph between F_0/F vs concentration of As^{3+} from 0 mM to 500 mM. (f) Plotting the linear range of As^{3+}detection.

From this linear range the LOD is determined to be 12.15 nM (Figure 3.9(f)). Interestingly, the linear range observed for As^{3+} detection is better than any reported in the literature. The data for LOD values and linear range for Hg^{2+} and As^{3+} ions are compared in Table 1 below. The LOD values are better or comparable to those reported in the literature.

Table 3. 2 LOD comparison of Hg^{2+} and As^{3+} ions with the other literature reported system.

Hg^{2+} Ions				
Precursor	**Detection Mode**	**Linear range**	**LOD**	**Ref.**

CQDs derived from ginkgo leaves	Turn - off	0.5–20 μM	12.4 nM	[191]
CQDs derived from lemon juice/ EDTA	Turn - off	0.001–1 μM	5.3 nM	[192]
CQDs derived from SnO2	Turn - on	0.02 - 100 μM	5 nM	[193]
Chl-a extracted from pea leaves in ethanol	Turn - off	2.0-10 μM	1.3 μM	[194]
sulfhydryl functionalized CQDs	Turn - off	0.45 - 2.1 μM	12 nM	[195]
Spinach chl-a extracted from peanut shell	Turn - off	-	8.5 mM	[196]
CQDs derived from phosphorus, sulfur, boron, and nitrogen atom	Turn - off	0.025-1500 mM	5 μM	[197]
CQDs derived from holly leaves	Ratiometric	0-100 μM	14 nM	[188]
CQDs derived from banana leaves	Turn-off	100-500 pM	67 pM	[85]
Our work	Turn-off	10nM-10μM	0.99 nM	
As^{3+} ions				
CQDs derived from thiol	Turn - off	5-100 ppb	0.086 ppb	[198]
CQDs derived from prickly pear cactus	Turn - off	2-12 nM	2.3 nM	[199]
CQDs and guanylated Poly (methacrylamide)	Turn - off	0.01-100 nM	247 pM	[200]
MPA-capped CdTe QDs and Rhodamine 6G	Turn - on	0.02-2 μm	6 nM	[201]
CdS–MAA QDs	Turn - off	0.08-3.20 mM	0.07 mg/L	[202]
CQDs derived from banana leaves	Turn-on	10-30 μM	1.5 μM	[85]
Our work	Turn-on	10-100μM	12.15 nM	

Our result indicates that CQD160 can be used as ON and OFF sensor for detecting As^{3+} and Hg^{2+} ions. In industrial sewages or other contaminated water resources multiple number of toxic metal ions may be present. So, if As^{3+} and Hg^{2+} ions are both present then how will the optical response of the CQD160 change? To answer this question, we recoded the PL spectra of CQD160 in the presence of both the As^{3+} and Hg^{2+} ions (Figure 3.10).

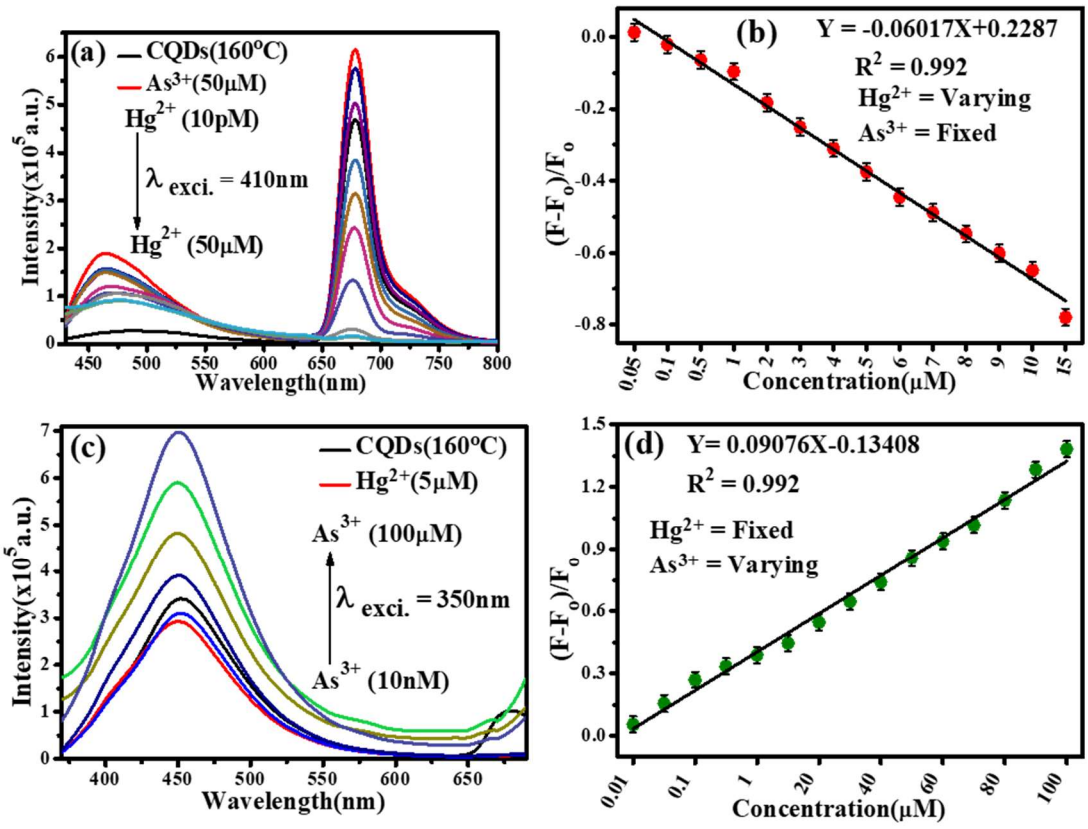

Figure 3. 10 Overlapping study of metal ions (Hg^{2+} and As^{3+}). (a) At fixed concentration of As^{3+} ions with different concentration of the Hg^{2+} ions. (b) Linear fitting of the Hg^{2+} over fixed As^{3+} ions concentration. (c) At fixed concentration of Hg^{2+} ions and varies As^{3+} ions concentration from 1o nM to 100 µM, (d) showing the linear fitting of the As^{3+} over the fixed concentration of Hg^{2+} ions.

The concentration of As^{3+} ions were fixed at 50µM while the concentration of Hg^{2+} was increased from 0µM to 50 µM (Figure 3.10(a)). We observe in the presence of As^{3+} ions the

rate of quenching of 676 nm peak is much faster with the peak completely vanishing at 50 μM of Hg^{2+} ion. Figure 3.10(b) shows the plot of F_0/F as function of Hg^{2+} ion when F_0 is the intensity of 676 nm peak for zero Hg^{2+} ion concentration and 50 μM As^{3+} concentration. Similarly, we observed for the concentration of Hg^{2+} ions were fixed at 5μM while the concentration of As^{3+} was increased from 10 nM to 100 μM (Figure 3.10(c) and 5(d)). For further validation, the CQDs were also used to test the presence of Hg^{2+} and As^{3+} in real water sample. Various real water samples were collected from different sources, including Ganga water from Assi Ghat, Varanasi (G-Water), tap water (T-Water), RO water, ground water from Badipur, Varanasi, India (GN-Water), and water from the Powai Lake (PL-Water from IITB Campus). Prior to testing, all water samples were filtered through a 0.22μm cyrine filter and heated at 100°C for 5 minutes to remove biological contamination. The fluorescence of the collected water samples was measured using the CQD160 probe, and the results were compared to a reference data set obtained from deionized (DI) water. From Figure 3.11(a) we see that the water collected from Powai Lake displayed highest fluorescence followed by water collected from river Ganga and then ground water. The fluorescence from DI water and RO water was the minimum[203]. 3.5μg/ml of CQD160 was added to all the water samples, the intensity of the peak around 450 nm increased and a new peak at 676 nm appeared (Figure 3.11(b)). When the emission spectra of all the water samples with CQDs with the control case (CQDs dispersed in DI water). Compared to DI water, the intensity of the 485 nm peak increased in all the real samples, while the intensity of the corresponding 676nm peak decreased with respect to the DI emission peak at 676nm. It indicates the presence of both As^{3+}ions and Hg^{2+} ions in real water samples. From the relative change in peak intensities, we can infer that the amount of A^{3+} ions in water samples collected from Powai Lake and river Ganga is much greater than the Hg^{2+} ions. From the relative change in peak intensities at 676 nm w.r.t the control case, we estimate around 3.62 μM of Hg^{2+}ions are present in Powai Lake. Determining the concentration of As^{3+}

ions present in the real water samples is not possible due to the presence of large fluorescence peak in these real water samples without CQDs. Similarly, real water sample testing through CQD220 and indicating the presence of As^{3+} ions (Figure 3.11(c) and (d)).

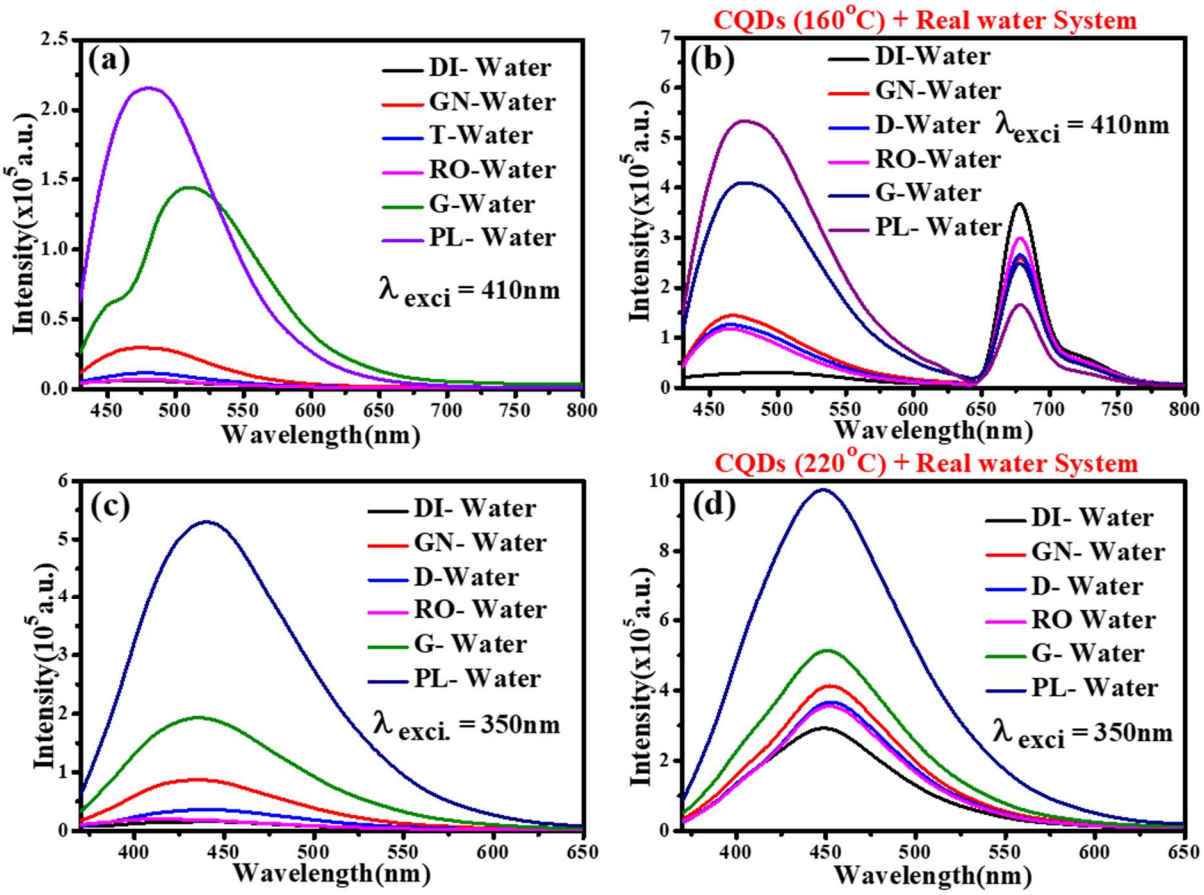

Figure 3. 11 Real water sample analysis. (a) and (b) PL emission spectra without and with CQD160 in various real sample using excitation 410nm. (c) and (d) PL emission spectra without and with CQD220 in real water system by exciting wavelength 350nm.

3.2.3 Quenching and Enhancement Mechanisms

For Hg^{2+} ions, the nonlinear SV plot shown in Figure 3.8(b) indicates the existence of both static and dynamic quenching. To verify the existence of dynamic quenching mechanism in the sensing process, TRPL spectroscopy technique was employed to investigate it. We monitored

the quenching dynamics of PL emission peak at 676 nm using an excitation of 370 nm. Figure 3.12(a) shows the TRPL for different concentrations of Hg^{2+} ions. The lifetime decay plots were fitted with second order exponential decay function as $y(t) = A_1 e^{-t/\tau_1} + A_2 e^{-t/\tau_2}$ [137]. We observe two decay constants τ_1 and τ_2 corresponding to two different quenching species. For the control case (without CQDs) we get τ_1 and τ_2 as 1.13 ns and 4.6 ns respectively with an average lifetime τ_{avg} of 2.12 ns. The variation of average lifetime as function of Hg^{2+} ion concentration is shown Figure 3.12(b). We observed a decrease in the average lifetime from 2.12 ns to 1.65 ns with an increase in the concentration of the Hg^{2+} ions. This confirms the presence of dynamic quenching during the sensing process. The linear plots were fitted with the equation (3.1).

$$\frac{\tau_0}{\tau} = 1 + K_q \tau_o [Q] \; = \; 1 + K_D [Q] \; \ldots\ldots\ldots\ldots\ldots\ldots (3.1)$$

where K_q, τ_o, τ, K_D, and Q are a biomolecular quenching constant, a lifetime without quencher, lifetime with the addition of quencher, dynamic quenching constant and concentration, respectively. From the linear fitting we could find the dynamic quenching constant K_D =8.0 x10^4 M^{-1} for Hg^{2+} ions. This high value of K_D indicates high fluorescence quenching efficiency. Now to verify the presence of static quenching we recorded the UV-Vis spectra of the CQDs after adding Hg^{2+} metal ions. Formation of non-fluorescent ground state complex between the fluorophore and the quencher is one of the factors responsible for static quenching. To confirm the formation of any non-fluorescent complexes UV Vis spectra of the CQDs after addition of Hg^{2+} ions were recorded. Figure 3.12(c) displays the UV-Vis absorption spectra of CQD160 with 10 µm and 100 µm Hg^{2+} ions. We observe that the intensity of the peaks around 300 nm, 417 nm and 676 nm decreases with the addition of Hg^{2+} ions. This correlates with the overall decrease in fluorescence intensity observed in the PL data. Thus, the UV-Vis absorption spectra

changes upon addition of Hg^{2+} ions, which indicate the formation of new ground state complex between CQDs and Hg^{2+} ions that blocks the usual fluorescence centres. The inset of Figure 3.12(c) shows the fluorescence being quenched when 10 µM and 100 µM of Hg^{2+} are added to CQDs under UV light illumination.

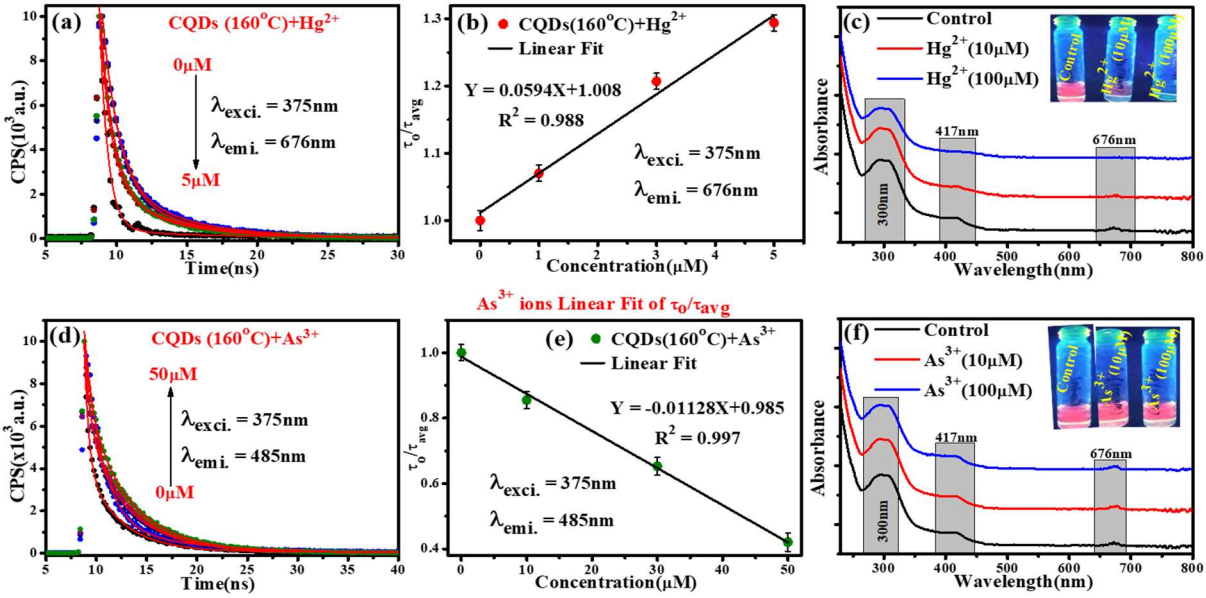

Figure 3. 12 (a), (c) TRPL spectra. (b), (d) plot of average lifetime. (c), (f) UV Vis spectra of CQDs(160ºC) with added Hg^{2+} and As^{3+}ions respectively.

For As^{3+} sensing system, we also monitored the dynamics of PL emission peak at 458 nm using an excitation of 370 nm. We observe an increase in lifetime as function of concentration. The plots were also fitted with bi-exponential function. The addition of As^{3+} resulted in an increase in the average lifetime from 1.55 to 3.68ns (Figure 3.12(d)). The lifetime values of τ_1 and τ_2 increased from 0.43ns to 0.96ns and from 3.52ns to 4.82ns, respectively with an average lifetime τ_{avg} of 1.55 ns (Figure 3.12(e)). The values of τ_1, τ_2, τ_{avg} and ratio of τ_0/τ_{avg} for Hg^{2+} ions and As^{3+} ions is shown in Table 3.3(a) and (b).

(a)

Concentration Hg^{2+}(μM)	τ_1(ns)	τ_2(ns)	τ_{av}(ns)	τ_o/τ_{av}
0	1.127	4.803	2.12	1
1	1.059	4.685	1.98	1.070
3	0.961	4.429	1.70	1.247
5	0.848	4.258	1.65	1.284

(b)

Concentration As^{3+}(μM)	τ_1(ns)	τ_2(ns)	τ_{av}(ns)	τ_o/τ_{av}
0	0.436	3.529	1.55	1
10	0.482	3.82	1.81	0.854
30	0.679	4.25	2.37	0.653
50	0.961	4.826	3.68	0.421

Table 3. 3 (a), and (b) Decay time of CQDs160 with and without addition of Hg^{2+} and As^{3+} ions.

We recorded the UV-Vis spectra of the CQDs after adding Hg^{2+} and As^{3+} metal ions. Figure 3.12(c) and (f) displays the UV-Vis absorption spectra of CQDs with Hg^{2+} and As^{3+}at 160ºC. There is no change in the UV-Vis spectra after addition of 10μM and 100μM of As^{3+} ions compared to the control (CQD160 with metal ions). It indicates that no new metal complexes are forming on addition of As^{3+} ions. However, for Hg^{2+} ions the UV-Vis spectra changes for 100μM of Hg^{2+} ions compared to the control. The absorption peak at 676 nm nearly vanishes while the peak at 425 nm reduces. The zeta potential of CQD160 was also measured in the presence of metal ions. Figure 3.13 shows the zeta potential of CQD160 with and without metal ions. The synthesized CQD160 without any metal ions exhibited a zeta potential of -27.4mV,

indicating the presence of electron rich surface functional groups, making it stable in the aqueous solution. However, upon addition of Hg^{2+}(10µM) and As^{3+}(10µM) ions, the zeta potential decreased to -20.7mV and -19.4mV, respectively.

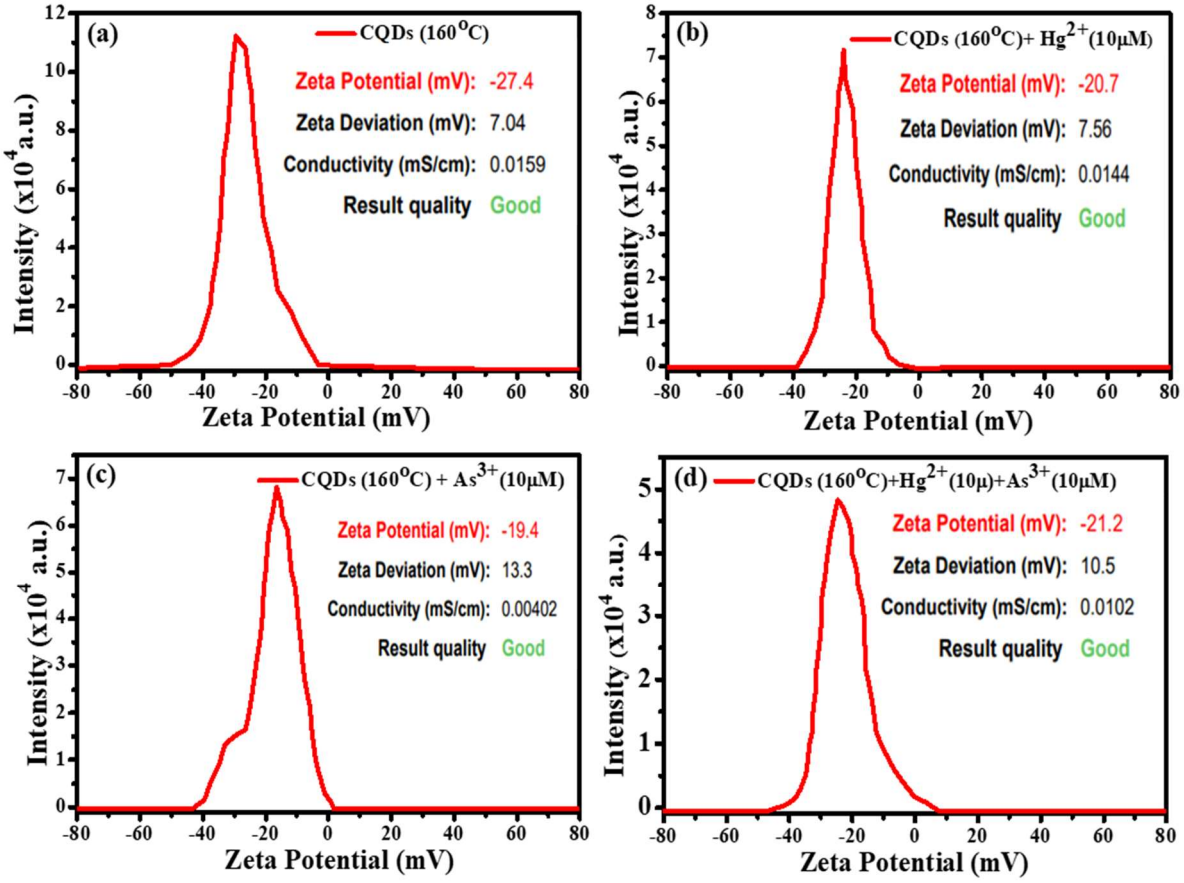

Figure 3. 13 Zeta potential behaviour with metal ions. (a) Zeta potential of synthesized CQDs160 in aqueous medium. (b), and (c) shows the zeta potential of CQDs160 with Hg^{2+}(10µM) and As^{3+}(10µM). (d) zeta potential of CQDs160 with mixed Hg^{2+}(10µM) and As^{3+}(10µM).

This decrease in the surface charge of CQD160 is due to interaction of the Hg^{2+} and As^{3+} ions with the functional groups.

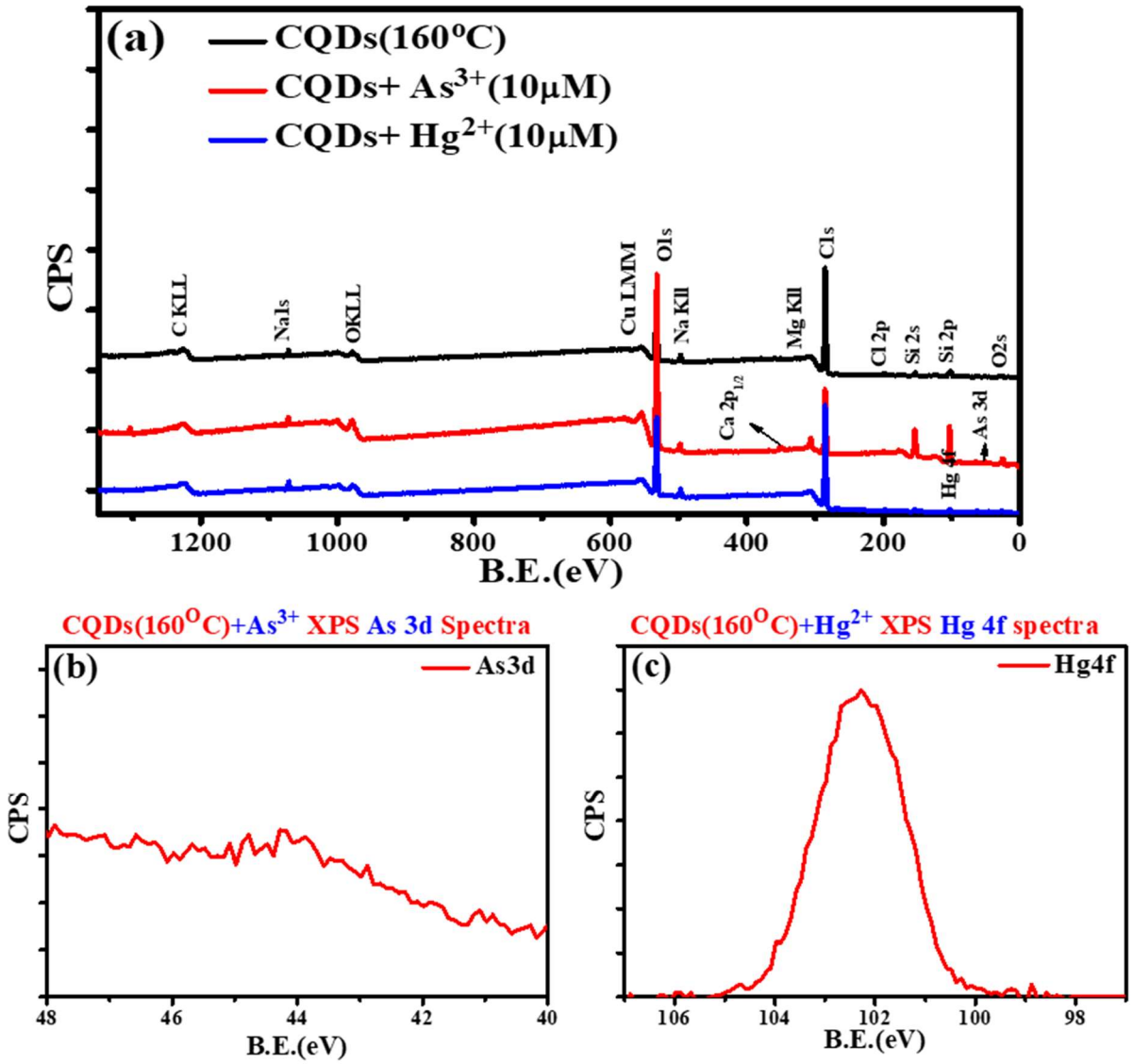

Figure 3. 14 (a) XPS survey spectrum of CQDs160 synthesized with metal ions (As^{3+} and Hg^{2+}) in range 0 to 1350eV. (b) High resolution XPS spectra of As3d. (c) High resolution XPS spectra of Hg 4f.

To understand the interaction mechanism further, we conducted FTIR and XPS measurement of the CQD with added Hg^{2+} and As^{3+} ions. Figure 3.15(a) shows the FTIR spectra of the CQD160 with 10 μM of As^{3+} and Hg^{2+}. From the FTIR spectra we observe a small change in the C=O stretching peak only. The XPS survey spectrum of CQD160 with Hg^{2+} and As^{3+} ions are shown in Figure 3.14(a) while the high resolution XPS spectra of As 3d and Hg 4f also shown in Figure 3.14(b) and (c). Figure 3.15(b), (c) and (d) shows high-resolution XPS spectra

of C1s, O1s and N1s peaks, respectively. In closer inspection, we can find out that in the case of C1s, the peak positions are shifting towards lower binding energy when the metal ions are added to the CQDs solution & the peak shape changes due to the increment in the graphitic contribution. A similar thing is happening for the O1s as well as for the N1s peaks.

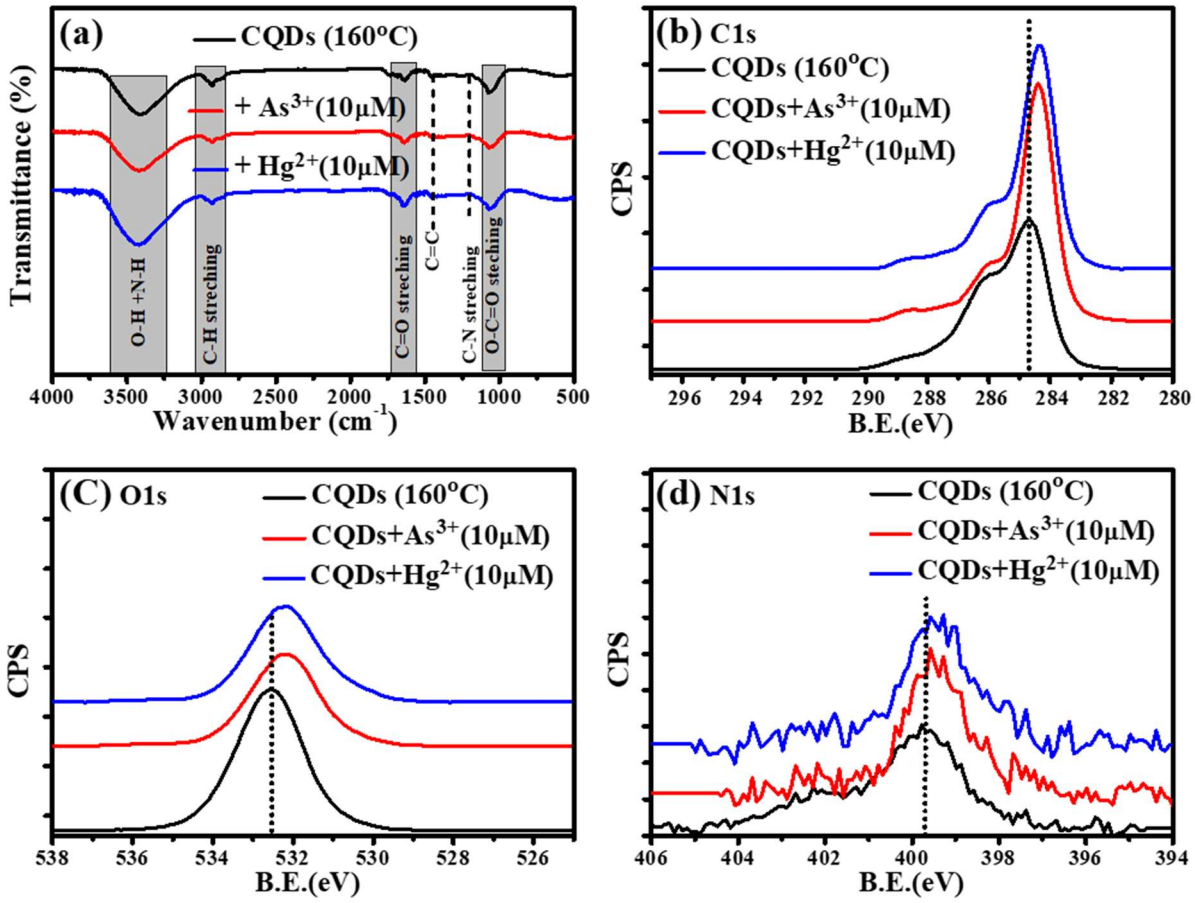

Figure 3. 15 (a) FTIR analysis of CQD160 prepared with metal ions (As^{3+}, and Hg^{2+}). (b), (c), and (d) shows the high resolution XPS photoelectron peaks of C1s, O1s, and N1s with metal ions (As^{3+}, and Hg^{2+}).

The high-resolution C1s, O1s & N1s peaks have been deconvoluted in the presence of Hg^{2+} and As^{3+} ions to investigate it further. The deconvolution & fitting of C1s, O1s & N1s peaks are shown in Figure 3.16.

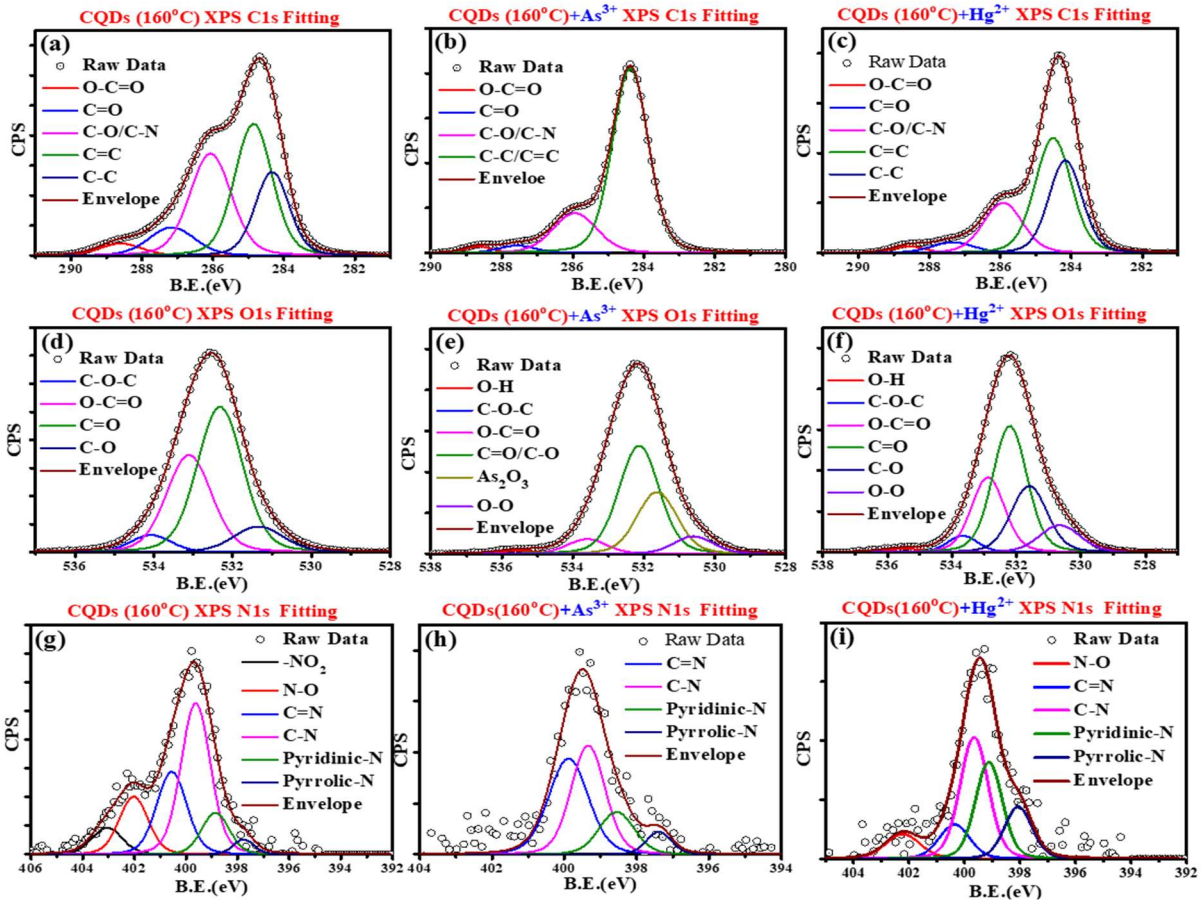

Figure 3. 16 Deconvolution of photoelectron XPS peaks with metal As^{3+} and Hg^{2+} ions. (a) CQDs160, (b) CQDs160 + As^{3+}(10μM), (c) CQDs160 + Hg^{2+}(10μM) shows the deconvolution of C1s photoelectron spectra. (d) CQDs160, (e) CQDs160 + As^{3+}(10μM), (f) CQDs160 + Hg^{2+}(10μM) shows the deconvolution of O1s photoelectron spectra. (g) CQDs160, (h) CQDs160 + As^{3+}(10μM), (i) CQDs160 + Hg^{2+}(10μM) shows the deconvolution of N1s photoelectron spectra.

For C1s, we observed the following bonding configuration, C-C/C=C, C-O/C-N, C=O & O-C=O, which is the same as the CQD160, but the concentration of these species changes abruptly. Upon the addition of As^{3+} and Hg^{2+} ion, the contribution from the graphitic species C-C & C=C increased from 50% to ~75% & concentration for the other bonding configurations C-O, C=O & O-C=O reduced from 40% to 23% (Table 3.4(a)).

(a)

C1s	CQDs-160°C+As3+		CQDs-160°C-Hg2+	
	Position (eV)	% Area	Position (eV)	% Area
C-O-C	--	--		
O-C=O	288.7	2.03	288.6	2.22
C-O-H	--	--		
C=O	287.6	3.08	287.4	4.56
C-O/C-N	285.9	19.90	285.9	19.98
C=C/C-C	284.4	74.99	284.5/284.2	42.14/31.09

(b)

O1s	CQDs-160°C+As3+		CQDs-160°C-Hg2+	
	Position (eV)	% Area	Position (eV)	% Area
O-H	535.5	1.11	535.5	1.24
C-O-C	533.6	5.08	533.7	4.50
O-C=O	532.8	27.68	532.9	22.69
C-O-H				
C=O/C-O	532.2	38.23	532.2	39.76
As_2O_3/ HG-O?	531.6	21.86	531.6	21.81
O-O	530.6	6.05	530.6	9.99

N1s	CQDs-160°C+As3+		CQDs-160°C-Hg2+	
	Position (eV)	% Area	Position (eV)	% Area
N-O	--	--	402.2	9.12
C=N	399.9	39.71	400.3	11.20
C-N	399.3	38.70	399.6	36.67
Pyridinic-N	398.6	15.67	399.1	27.63
Pyrrolic-N	397.4	5.92	398.0	15.38

Table 3. 4 Deconvolution of Different functional groups of (a) C1s, (b) O1s, and N1s.

For O1s, we observed O-O, As_2O_3, C-O/C=O, O-C=O, C-O-C & O-H. From the deconvolution of O1s spectra, it is clearly observed that when the As^{3+} & Hg^{2+} ions are added to the CQD solution, the ions are more prone to bind with oxygen atoms & resulting in the formation of As_2O_3. As a result, oxygen species in the solution decreased & leftover carbon atoms increased the graphitic contribution in the solution (Table 3.4(b)). Similar things also can be seen for the N1s peak, where the concentration of oxygen-rich -NO & $-NO_2$ configurations have also been reduced (Table 3.4(c)).

3.2.4 Biocompatibility and Bioimaging of CQDs

NIH-3T3 cells were exposed with CQDs nanoparticles at a concentration of 80, 160, 240 and 320 µg/mL for 24, 48, 72 hrs and cytotoxicity were determined using MTT assay. Figure 3.17(a) and (b) illustrate the dose and time dependent cytotoxicity and viability of CQDs in NIH-3T3 cells at 24hrs, 48hrs and 72hrs.

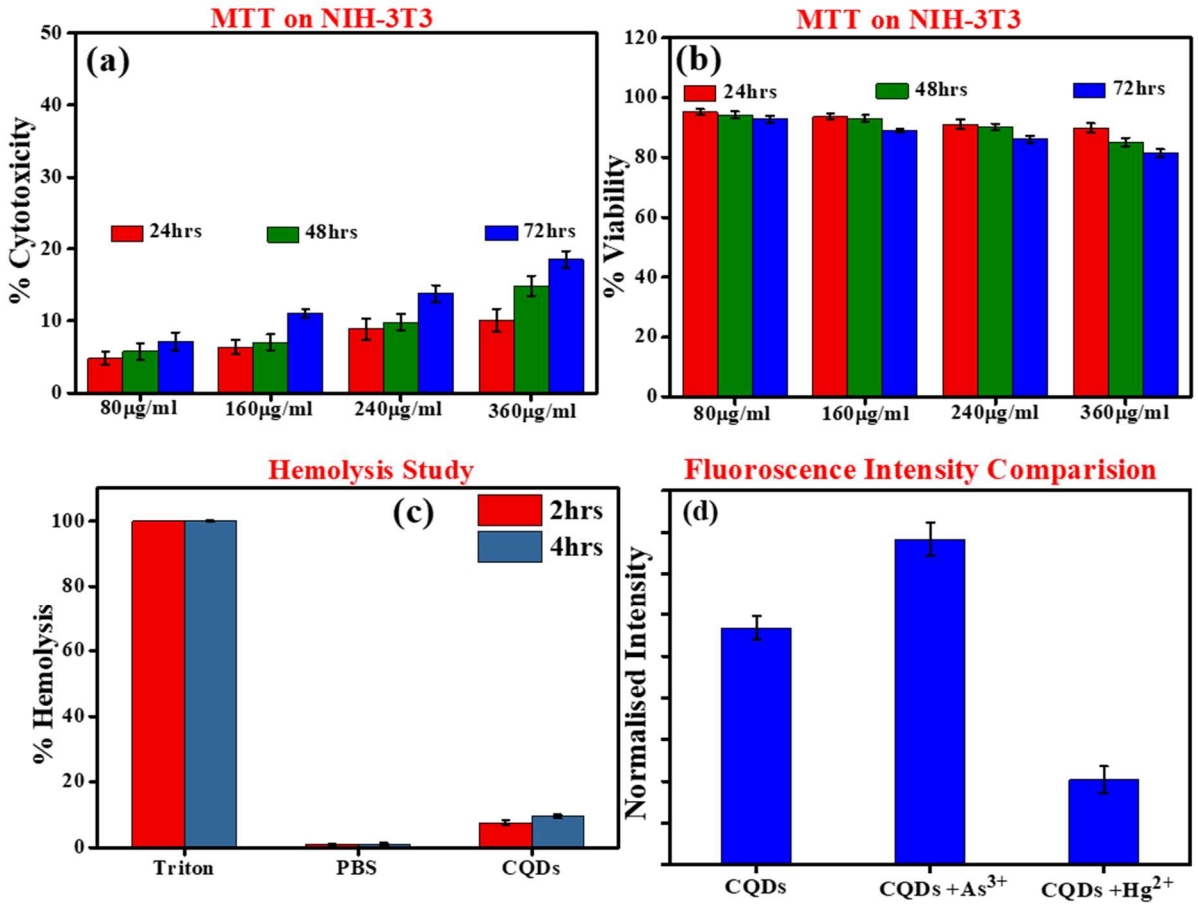

Figure 3. 17 (a), and (b) shows the % cytotoxicity and % viability of CQD160 on NIH-3T3 cell line after 24 hrs, 48 hrs and 72 hrs, (c) *Ex vivo* hemolysis activity of CQD160 after 2 and 4 hrs, (d) fluorescence intensity of CQD160 and CQD160 with As^{3+} and Hg^{2+} in NIH-3T3 cell line post 2 hrs of treatment.

There is almost negligible cytotoxicity at low to high concentration of nanoparticles after 24 hrs and 48 hrs, while less than 20% cytotoxicity at higher concentration of nanoparticles even after 72 hrs of incubation. The cell viability of CQD160 in NIH-3T3 cell lines was found to be as high (80-90%) at 80 µg/mL, 160 µg/mL, 240 µg/mL, 320µg/mL , after 24hrs, 48hrs and

72hrs of incubation time that confirmed the biocompatibility of nanoparticles even at higher concentration. *Ex-vivo* biocompatibility of CQD160 was evaluated by hemolysis assay, by incubating them with human blood for 2 and 4hrs (Figure 3.17(c)). Almost negligible hemolysis was detected in all experimental groups compared to that of positive control (Triton-X) proving their biocompatibility with red blood cells at both the time intervals. Nanoparticles such as gold nanoparticles, silver nanoparticles, and CdTe nanoparticles have been widely used in biosensing assays, but their toxicity has been a concern. To overcome this issue, biocompatible materials have gained more attention. In this study, we employed biocompatible CQD160 for a fluorescent-based biosensing assay. The assay relies on analysing the fluorescence intensity of CQD160 with respect to heavy metals such as $As^{3+}$and Hg^{2+} ions. The conjugation of CQD160 with As^{3+}or Hg^{2+} ions can result in changes in the fluorescence of CQD160. The fluorescence behaviour changes due to the formation of a non-fluorescent fluorophore after the addition of Hg^{2+} ions. However, in the case of As^{3+}ions, the PL intensity is enhanced by the electron transfer process. By analysing these variations in fluorescence, the conjugation of As^{3+}or Hg^{2+} with CQD160 can be determined, and the presence of these metals in the cells/sample can be detected. For the meantime, Figure 3.18 depicts the changes in fluorescence that result from conjugation of As^{3+}or Hg^{2+} with CQD160 in pre-treated NIH-3T3 cells. As can be seen, there is no self-fluorescence of $As^{3+}$and Hg^{2+} while CQD160 showed prominent self-fluorescence in both cytoplasm as well as in nucleus. Figure 3.17(d) depicted that the cells treated with $As^{3+}$and Hg^{2+} ions produce changes in fluorescence intensity when compared with CQD160 alone. However, treatment of cells with CQD160 and Hg^{2+} showed stronger quenching of fluorescence intensity as compared to CQD160 alone. Based on above results, this fluorescence based biosensing can be used to detect the presence of these metals in a system.

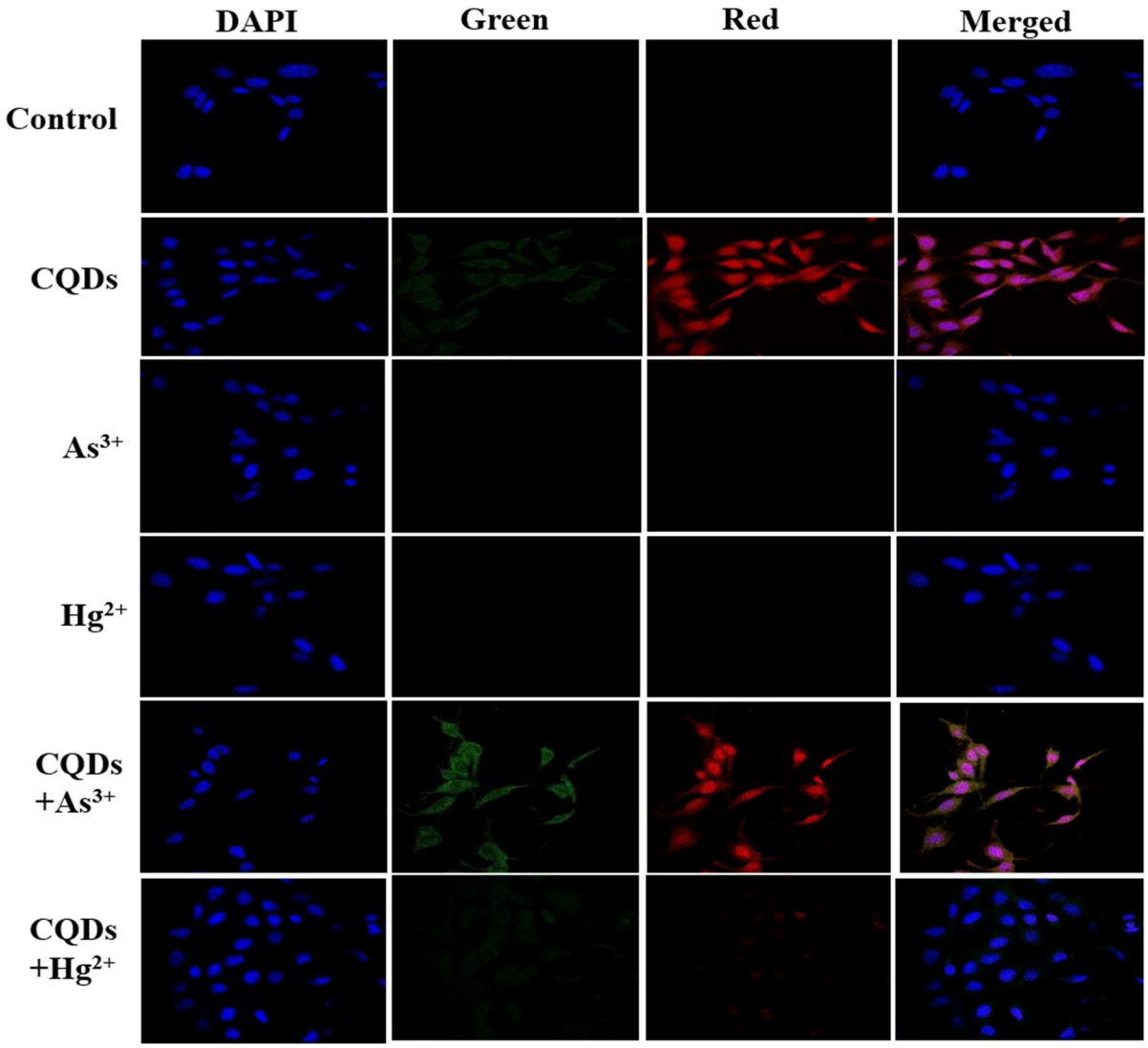

Figure 3. 18 Confocal microscopy of control, CQDs, As^{3+}, Hg $^{2+}$, and mixed on pre-treated NIH-3T3 cell line post 2hrs of treatment.

3.3 Conclusion

In summary, we succeeded in synthesizing chlorophyll-rich CQDs via a one-step solvothermal method and in producing an efficient fluorometric sensor for the simultaneous detection of Hg^{2+} and As^{3+} ions. The ingenious strategy was to use Plumeria plant leaves as precursors for the synthesis of CQDs. The synthesized CQD160 showed excellent pH, salt and storage stability. In addition, fluorometric sensing showed high sensitivity and selectivity towards Hg^{2+} and As^{3+} ions. The detection limit (LOD) for Hg^{2+} and As^{3+} metal ions in the DI solution was

reported to be 0.99 nM and 12.15 nM, respectively. The proposed probe showed significant results in a real water system and estimated the Hg^{2+} ion concentration to be 3.62 mM in Powai Lake. The fluorescence lifetime measurements showed that the quenching of fluorescence upon addition of Hg^{2+} ions was due to a combination of static and dynamic quenching mechanisms. We were able to determine the dynamic quenching constant K_D=8.0 x104 M^{-1} for Hg^{2+} ions. This high value of K_D indicates high efficiency of fluorescence quenching. To understand the effects of the metal ions on the fluorescence of the CQD160, we investigated the interaction of the metal ions with the CQD160 using X-ray photoelectron spectroscopy. We observe that the Hg^{2+} and As^{3+} ions are binding to oxygen functional groups present on the CQDs which alters the fluorescence of the CQDs. The CQD160 were found to be biocompatible and less cytotoxic, providing excellent bioimaging in the blue, green, and red regions. We also used these CQD160 to detect As^{3+} and Hg^{2+} ions in human cells NIH-3T3 and also performed a hemolysis study.